Comparison of Dislocation Characterization by Electron Channeling Contrast Imaging and Cross-Correlation Electron Backscattered Diffraction

Bret E. Dunlap[a], Timothy J. Ruggles[c], David T. Fullwood[b], Brian Jackson[b], Martin A. Crimp[a,*]

[a] *Chemical Engineering and Materials Science, Michigan State University, East Lansing, MI 48824, USA*
[b] *Mechanical Engineering, Brigham Young University, Provo, UT 84602, USA*
[c] *National Institute of Aerospace, Hampton, VA 23662, USA*

Abstract

In this work, the relative capabilities and limitations of electron channeling contrast imaging (ECCI) and cross-correlation electron backscattered diffraction (CC-EBSD) have been assessed by studying the dislocation distributions resulting from nanoindentation in body centered cubic Ta. Qualitative comparison reveals very similar dislocation distributions between the CC-EBSD mapped GNDs and the ECC imaged dislocations. Approximate dislocation densities determined from ECC images compare well to those determined by CC-EBSD. Nevertheless, close examination reveals subtle differences in the details of the distributions mapped by these two approaches. The details of the dislocation Burgers vectors and line directions determined by ECCI have been compared to those determined using CC-EBSD and reveal good agreement.

Keywords: ECCI, CC-EBSD, HR-EBSD, EBSD dislocation microscopy, Dislocations, Nanoindentation

1. Introduction

To understand how polycrystals deform and develop damage that leads to fracture, it is necessary to characterize the dislocations involved in the underlying plastic deformation. This dislocation content is made up of both the statistically stored dislocation (SSD) content, consisting of the portion of the overall dislocation density that effectively cancels itself out, i.e. due to dislocation dipoles, and the geometrically necessary dislocations (GNDs) that are associated with the crystal elastic strain gradients that develop through plastic deformation.

Traditionally, dislocation structures have been characterized using transmission electron microscopy (TEM) [1, 2]; however, TEM is plagued by a number of limitations associated with the requisite thin foils. These can include difficult sample preparation, the potential for this sample preparation to affect the apparent dislocation distributions, and limited observation volumes can lead to poor statistical representation of the bulk.

Two significantly different techniques, electron channeling contrast imaging (ECCI) [3–8] and cross-correlation electron backscattered diffraction (CC-EBSD) [9–12], are alternative scanning electron microscopy (SEM) based approaches for characterizing dislocation structures. Both of these techniques involve the examination of the near surface region of bulk samples and require careful preparation of this surface region to be examined; nevertheless, eliminate many of the limitations imposed by TEM thin foils. Surface preparation may be carried out either before or after the imposed deformation.

In many respects, ECCI is carried out in the same manner as diffraction contrast TEM; that is, imaging is achieved by setting up specific diffraction/channeling conditions. Instead of using electron diffraction patterns to establish "2-beam" conditions as with TEM, ECCI relies on either electron channeling patterns (ECPs), selected area channeling patterns (SACPs), or EBSD patterns to establish electron channeling conditions [3, 8, 13]. This allows dislocations to be characterized in terms of their Burgers vectors, **b**, and line directions, **u**, using the well established $\mathbf{g} \cdot \mathbf{b} = 0$ and $\mathbf{g} \cdot \mathbf{b} \times \mathbf{u} = 0$ invisibility criterion, where **g** describes the channeling condition [3–5]. The dislocation line widths resolved by ECCI are similar to that offered by diffraction contrast bright field imaging TEM, in the range of 10 to 12 nm[8]; however, TEM has the advantage of weak beam microscopy which decreases the dislocation line width, allowing TEM to image areas with high dislocation densities [14, 15]. Conversely, ECCI has the advantage of only having one free surface, so that image force [16] effects will not be as severe as in TEM thin foils.

CC-EBSD, also referred to as high resolution or high angular resolution EBSD [10–12], is a recently developed approach for mapping the GND content deduced from the Nye tensor [17]. Components of the Nye tensor come from elastic distortion gradients, determined from subtle shifts in the EBSD patterns between neighboring pixels in an EBSD map [9, 10].

To fully exploit the ECCI and CC-EBSD approaches, it is important to establish the limitations and relative capabilities of these techniques. A number of papers have shown how ECCI and CC-EBSD can be used in complement of each other for a better analysis of dislocation structures [12, 18, 19]. Vilalta-Clemente et al. [19] used CC-EBSD to characterize relatively low density threading dislocations in as-grown InAlN epitaxial thin films, determining the individual densities for pure edge, pure screw, and mixed threading dislocations using supplemental information from ECCI; however, CC-EBSD and ECCI were carried out in different areas of the same sample. This work also indicated that the sign of individual dislocations could be assessed by CC-EBSD.

The objective of the present study is to directly compare dislocation structures characterized by ECCI and CC-EBSD in the same area. These observations have been carried out by examining the dislocation fields developed around nanoindentations in body centered cubic (bcc) Ta. Of particular interest is the comparison between the information available from CC-EBSD and ECCI and the establishment of CC-EBSD as a viable technique for the rapid determination of GND densities, including its ability to characterize the specific slip systems involved in deformation.

2. Materials and Methods

To obtain sufficient sample quality for ECCI and CC-EBSD, a polycrystalline sample of undeformed high purity Ta was metallographically prepared by grinding in steps down through 4000 grit SiC. A final polish was achieved using a 4 to 1 mixture of Struers OP-S and aqueous 30 % H_2O_2 on a Struers MD-Chem polishing cloth.

EBSD mapping of the polished material was carried out using a Tescan Mira 3 FEG-SEM and an EDAX Hikari EBSD camera with a 480 × 480 pixel resolution and Orientation Imaging Microscopy software (OIM^{TM}). Nanoidentation was performed using an MTS Nano Indenter. A 25 × 22 array of nanoindents with 10 µm spacing was placed in the material, resulting in a large number of indentations that were well-isolated from grain boundaries and a few indents located close to grain boundaries. All of the indention was performed with a maximum load of 4 mN and a 10 s load- 10 s hold- 10 s unloading cycle. In order to avoid anisotropies associated with the tip geometry, indentation was carried out using a spherical conical tip with an ∼1 µm tip radius.

ECCI was carried out using the Tescan Mira 3 at 30 kV, a working distance of approximately 9 mm, an instrument spot setting of 6.1 nm, and a specimen current of 2.2 pA. Specific channeling conditions were established using selected area channeling patterns (SACPs) facilitated by the beam rocking function. Channeling imaging conditions were established through a combination of stage rotations and tilts determined using the TOCA software package [20].

EBSD patterns for cross-correlation analysis were collected around the same indentation regions that were examined with ECCI, using step sizes of 100 nm, 50 nm, and 25 nm. Patterns for cross-correlation were captured using the same Tescan SEM and EDAX Hikari EBSD system. To acquire EBSD patterns with high contrast and low noise, necessary for cross-correlation analysis, an instrument spot size of 20.0 nm and specimen current of 1.9 nA was used with an exposure time of 0.1 sec. The patterns were not binned, but the 480×480 pixel resolution used is comparable to 2×2 binning for cameras that have 1000×1000 pixel resolution.

Neighboring patterns were then cross-correlated in two directions using the OpenXY software [21] to obtain the relative elastic distortion between the crystal lattices at the relevant scan points [22]. The resulting distortion gradients provide 12 of the necessary 18 derivatives required for the Nye tensor (the basis of continuum dislocation theory). Since the calculated GND density is sensitive to the chosen scan step size, the software allows selection of a step size that is a multiple of the original scan step size; i.e. the cross-correlation calculation for distortion gradient can be calculated between nearest neighbor points, next-nearest neighbor points, etc; resulting in a range of effective step sizes. Ruggles et al. [22] discussed the necessity to find a range of effective step sizes, where the associated GND densities become relatively constant in order to accurately determine the "true" GND density; for Ta, they found this range to be between 100 nm and 200 nm.

To determine the necessary effective step size for calculating GND densities for this work, an EBSD scan was collected with a 25 nm step size and GND densities were calculated using effective step sizes between 25 nm and 400 nm, shown in Fig. 1 as box plot distributions of measured densities for each effective step size. At an effective step size of 175 nm, Fig. 1 shows that GND densities enter a region where they become relatively constant, in agreement with the results by Ruggles et al. [22].

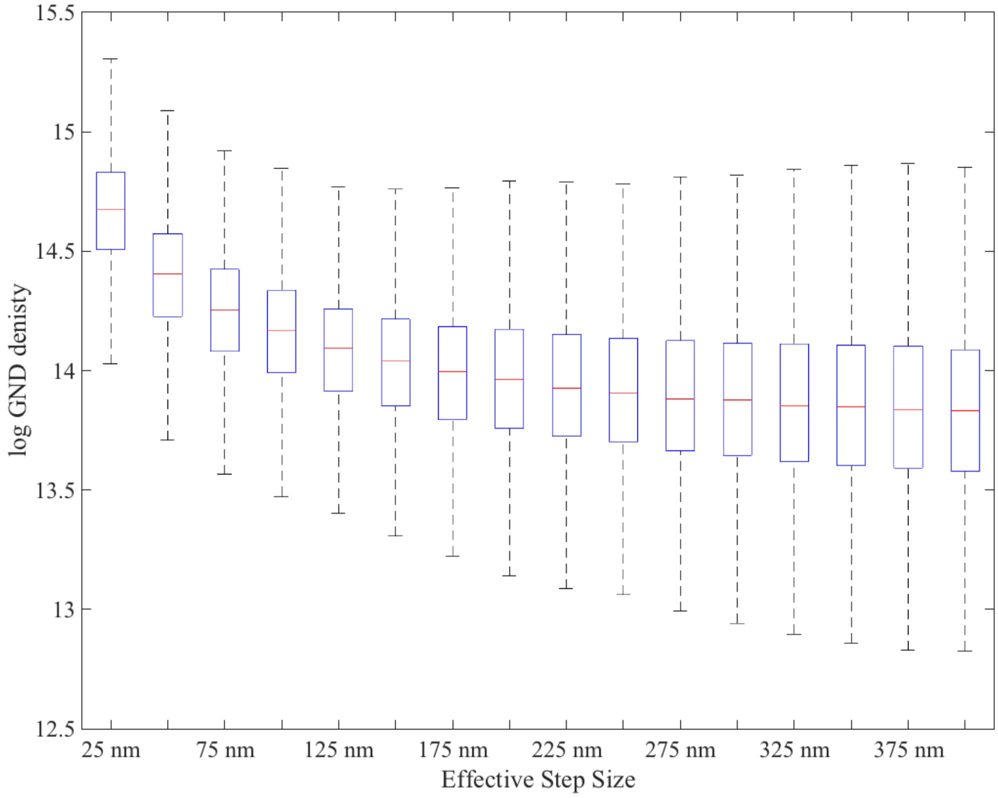

Figure 1: Box plots showing GND density distributions for effective step sizes between 25 nm and 400 nm.

3. Results

3.1. Dislocation Distributions

The dislocation distribution around an indent well isolated from the grain boundaries (a "single crystal" indent) in a grain oriented near [0 1 1] was analyzed. Fig. 2a, which was produced by stitching multiple ECC images together, shows the general deformation fields around the indent. The strong intensity near the edge of the indentation can be attributed to the nominally tear shaped backscattered electron interaction volume escaping from the interior surface of the indent when the electron beam is scanned close to the edge of the indent. This effect is most likely complicated by the extensive deformation and localized rotations expected near the indent. Furthermore, the bright region appears asymmetrical due to the sample being tilted. Moving away from the high intensity region, dislocation fields extend from the indent in a number of directions. Most of the dislocations in these fields appear as black/white dots, representing dislocations roughly normal to the surface (examples shown in the dashed circle in Fig. 2a), but some appear more extended due to their lines being more parallel to the surface (example shown in dashed rectangle in Fig. 2a). More detailed images showing individual dislocations are illustrated in subsequent figures. The corresponding CC- EBSD calculated GND map (total GND density), shown in Fig. 2b, displays dislocation distributions comparable to those in the ECC image. The pixels that correspond to EBSD patterns that have a confidence index less than 0.15 are whited-out.

3.2. Dislocation Density Comparison

A more detailed comparison between the ECCI and CC-EBSD results, carried out on a neighboring indent within the same grain, is shown in Fig. 3. Here the ECCI, Fig. 3a, shows a broad band of dislocations extending to the upper left of the indent and a fainter band near the right hand edge of the image, which curves to the left moving up in the image. Individual dislocations can be readily discerned, with the majority of the dislocations appearing close to end-on in the image. As before, there are also smaller numbers of dislocations with line directions more parallel to the sample surface. A comparison of this image with the corresponding GND map from CC-EBSD, Fig. 3b, again shows good agreement with the approximate locations of the dislocations. Nevertheless, there is not an exact one-to-one correlation between ECCI and the CC-EBSD images for reasons which will be discussed below.

In order to facilitate a robust comparison, the dislocation locations determined from the ECC image in Fig. 3a, have been plotted with the same step-size and color scale as the CC-EBSD map, with the color scale now reflecting the number of dislocations per unit area of a pixel (an effective dislocation density) in Fig. 3c. Regions where dislocations could not be reliably imaged, i.e. the indent rim and inside the indent, were whited-out, seen in the lower right in Fig. 3c.

3.3. Dislocation Characterization Using ECCI

The dislocations imaged using ECCI were characterized using channeling contrast criteria supplemented with the approximate line directions [5–8]. This analysis is focused on the region outlined by white dashes in the upper left portion in Fig. 4a. This image, collected using the $\mathbf{g} = (\bar{2}\,1\,\bar{1})$ channeling condition, shows what appears to be 64 dislocations in the circled region,

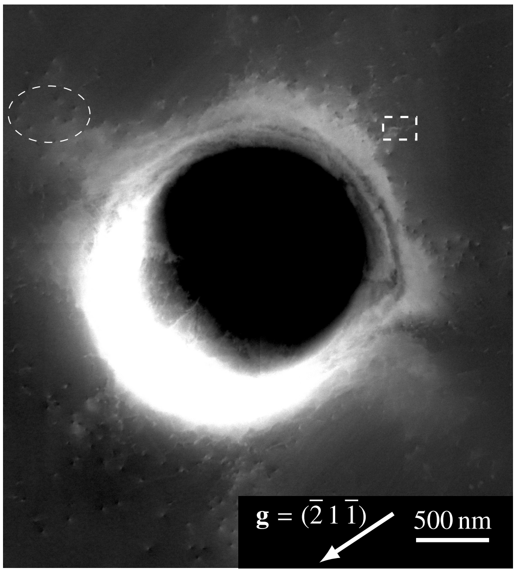

(a)

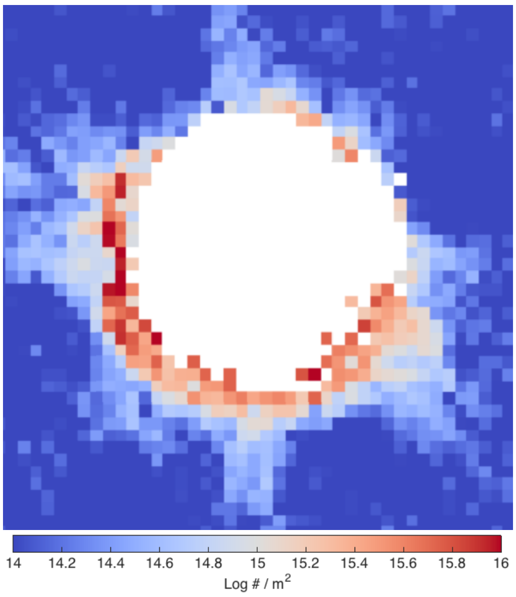

(b)

Figure 2: (a) Multiple ECC images stitched together showing dislocations generated from a nanoindenation in a grain of approximately [0 1 1] orientation. (b) CC-EBSD GND map of the same area, collected with an EBSD scan step size of 100 nm and effective step size of 200 nm, showing dislocation distributions similar to that in the ECC image.

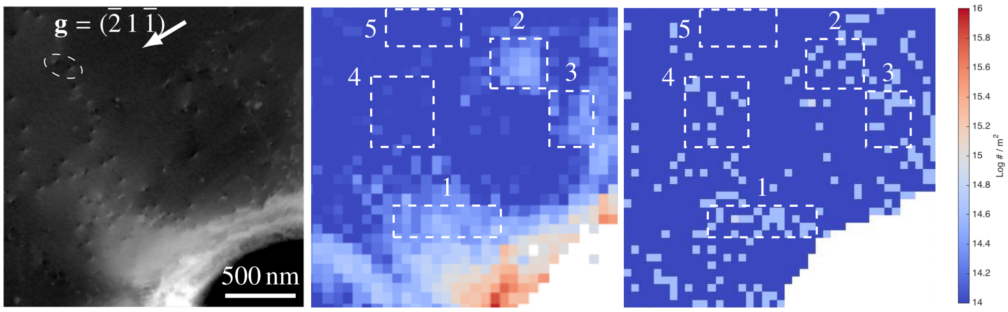

(a) (b) (c)

Figure 3: (a) ECC image of dislocations from the upper-left of the indented area. (b) CC-EBSD generated GND density map of the same area showing similar dislocation distributions, using a step size of 50 nm and an effective step size of 200 nm. (c) Dislocation density map calculated by counting dislocations in the ECC image.

(in a few cases the contrast is complicated and may represent more than one dislocation). Careful examination of these dislocations reveals that many of them have their characteristic black/white contrast in the same orientation, while others display reversed or rotated contrast. These differences in contrast can indicate different Burgers vectors and/or edge or screw type dislocations [1, 23, 24]. Overall, 39 of the dislocations reveal the same contrast orientation, with four having reversed contrast. An additional 21 display different contrast orientation or are difficult to categorize due to weak contrast.

The six different channeling conditions used for the analysis shown in Fig. 4 were established by rotating and tilting the sample in conjunction with SACPs. The majority of dislocations do not go out of contrast with any of the channeling conditions, but the orientation of the black/white contrast varies with each channeling condition. The fact that the dislocations do not go out of contrast suggests that these are screw dislocations that are generally perpendicular to the surface. That is, despite the fact that $\mathbf{g} \cdot \mathbf{b} = 0$ for all of the $\mathbf{g}$ vectors perpendicular to the screw line direction, the surface relaxation causes them to always be visible [2]. The white dashed arrows in Fig. 4 shows that the direction of the black to white contrast is roughly perpendicular to $\mathbf{g}$, consistent with the contrast expected from screw dislocations generally perpendicular to the surface [1, 23, 24].

The four possible $\langle 1\ 1\ 1 \rangle$ screw dislocation line directions in this region are each shown as an "x" on the stereographic projection with respect to the back-scatter detector, shown in Fig. 5a.

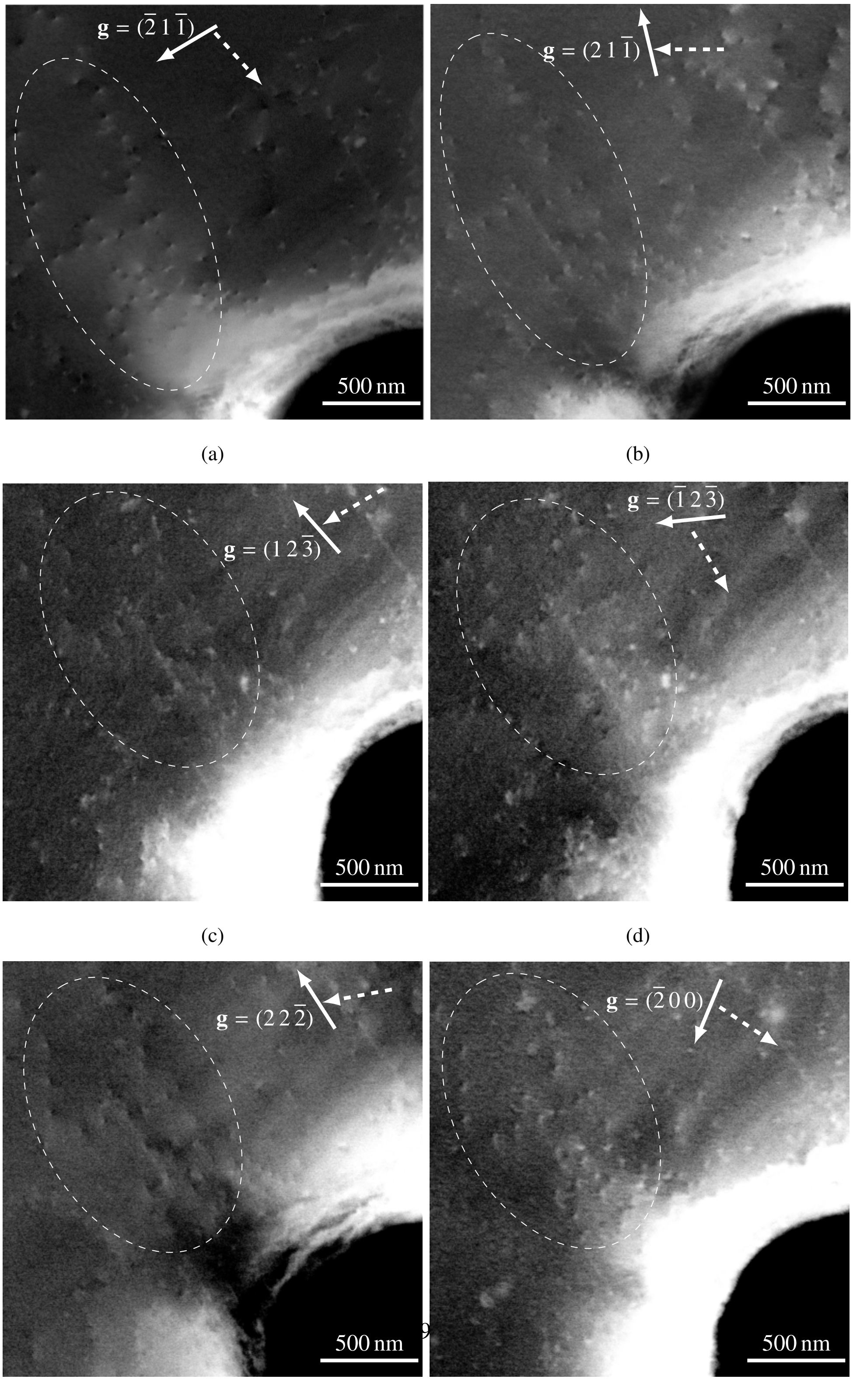

Figure 4: ECC images for the channeling conditions used for contrast analysis, with **g** indicated by the white arrows and the black to white contrast indicated by the white dashed arrows.

Two of these line directions, the $[1\,\bar{1}\,1]$ and $[\bar{1}\,\bar{1}\,1]$, are nearly parallel and can be eliminated as potential Burgers vectors/line directions of the dislocations that are close to perpendicular. To distinguish between the two remaining possibilities, $[1\,1\,1]$ and $[\bar{1}\,1\,1]$ (which are 40° and 31° from perpendicular to the beam axis, respectively), the sample was tilted 11° along $\mathbf{g} = (\bar{2}\,1\,\bar{1})$, with the resulting orientation shown in the stereographic projection in Fig. 5b. This tilt would cause $[1\,1\,1]$ screw dislocations to become more parallel to the detector (48° from the beam axis) while $[\bar{1}\,1\,1]$ screw dislocations would become more perpendicular to the detector (27° from the beam axis). The ECC image corresponding to this tilt, Fig. 5c, shows the dislocations now projecting as lines that project (fade) towards the bottom of the image, indicating the majority of the dislocations have line directions close to $[1\,1\,1]$. Combined with the sense of contrast discussed above, it is reasonable to conclude that these most common dislocations are $a/2\,[1\,1\,1]$ screw dislocations. It is worth noting that the other dislocations that display different black/white contrast do not project in the same direction as the $a/2\,[1\,1\,1]$ screws, suggesting they have different line directions and Burgers vectors.

3.4. Dislocation Characterization Using CC-EBSD

In addition to the total dislocation density shown in previous sections, the Nye tensor determined from CC-EBSD analysis may also be used to characterize the Burgers vector and edge/screw character of the local dislocation density, as well as the slip plane of the edge dislocations (the slip plane of screw dislocations is not determinable because it has no effect on the Nye tensor) via the Nye-Kröner method. The GND densities were determined using the line length minimization approach outlined by Ruggles et al. [25]. For this analysis, the smallest available effective step size of 25 nm was employed to maximize the spatial resolution of the method. The dislocation densities of each screw and edge dislocation possibility are shown in Fig. 6. The dislocation densities were locally averaged to better show trends. In the highly deformed region near the indent, the Nye-Kröner method identifies the Burgers vector of dislocation content where ECCI was incapable of resolving dislocations. In the region further from the indent, where individual dislocations were discernible via ECCI, CC-EBSD also characterized the dislocation content as being composed of screw dislocations with a $[1\,1\,1]$ Burgers vector. To highlight agreement with the two methods, the dislocation density for the $[1\,1\,1]$ screw dislocation determined via CC-EBSD is shown in greater detail in Fig. 7.

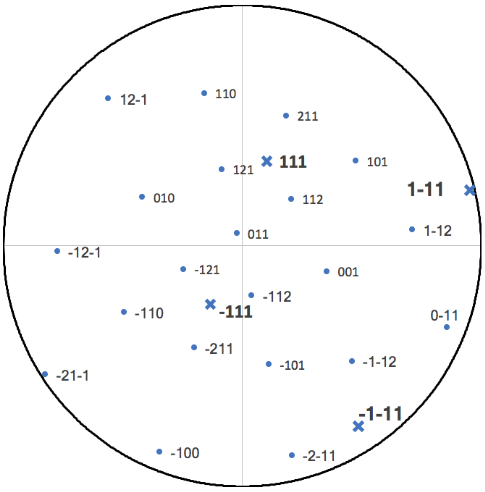

(a)

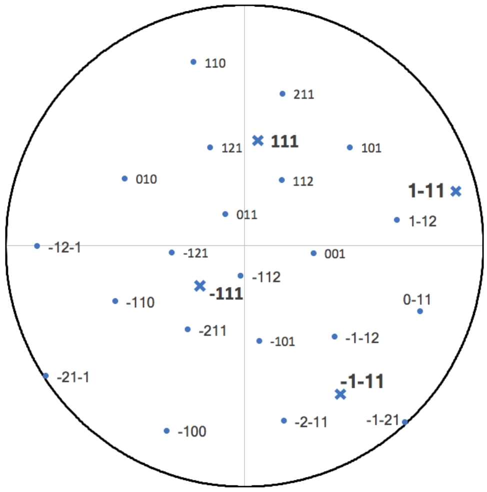

(b)

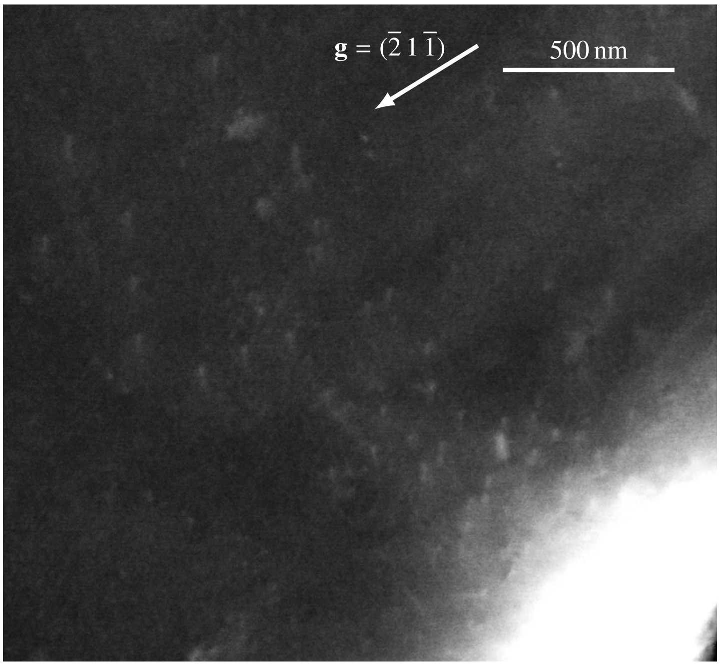

(c)

Figure 5: Stereographic projections (a) corresponding to Fig. 4a and (b) tilted 11° along the $\mathbf{g} = (\bar{2}\,1\,\bar{1})$ with each "x" being a line direction for the four possible screw dislocations. (c) ECC image with the same sample tilt as in (b), showing a projection of the dislocation line directions.

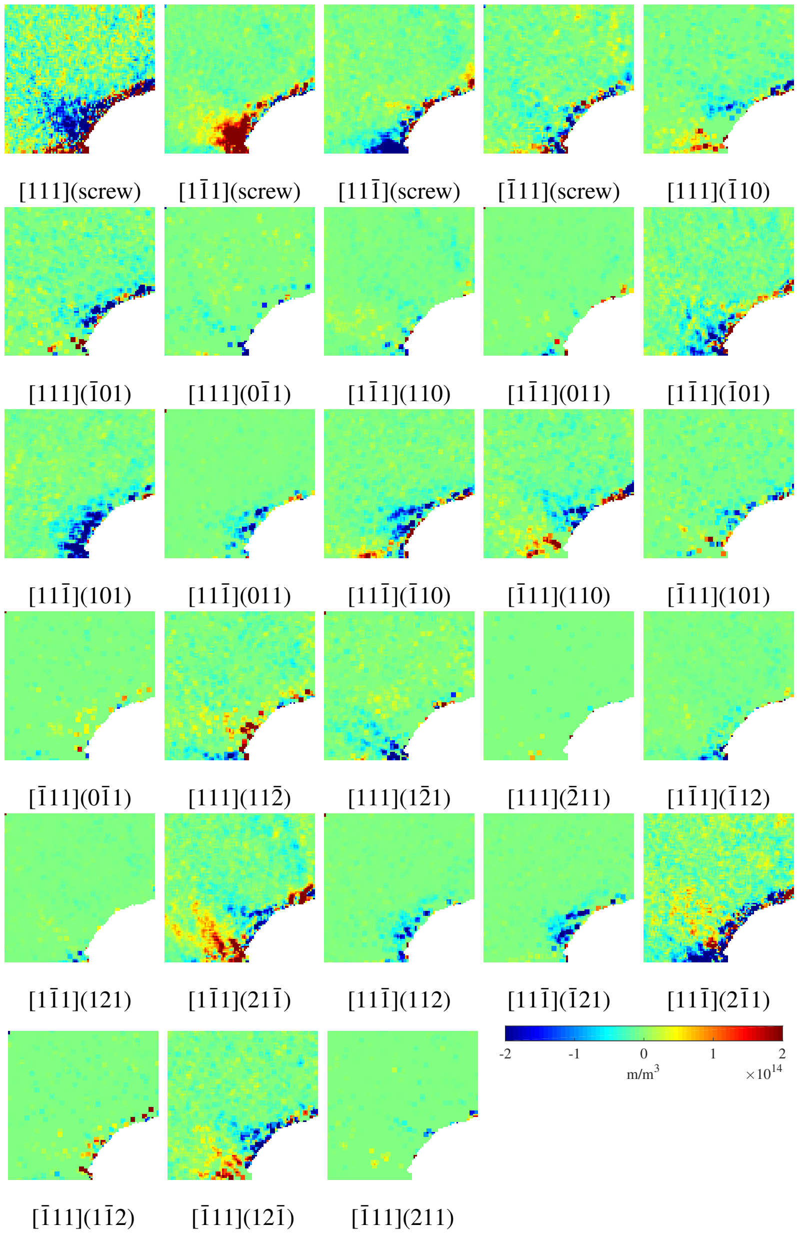

Figure 6: Dislocation density of each dislocation type according to CC-EBSD.

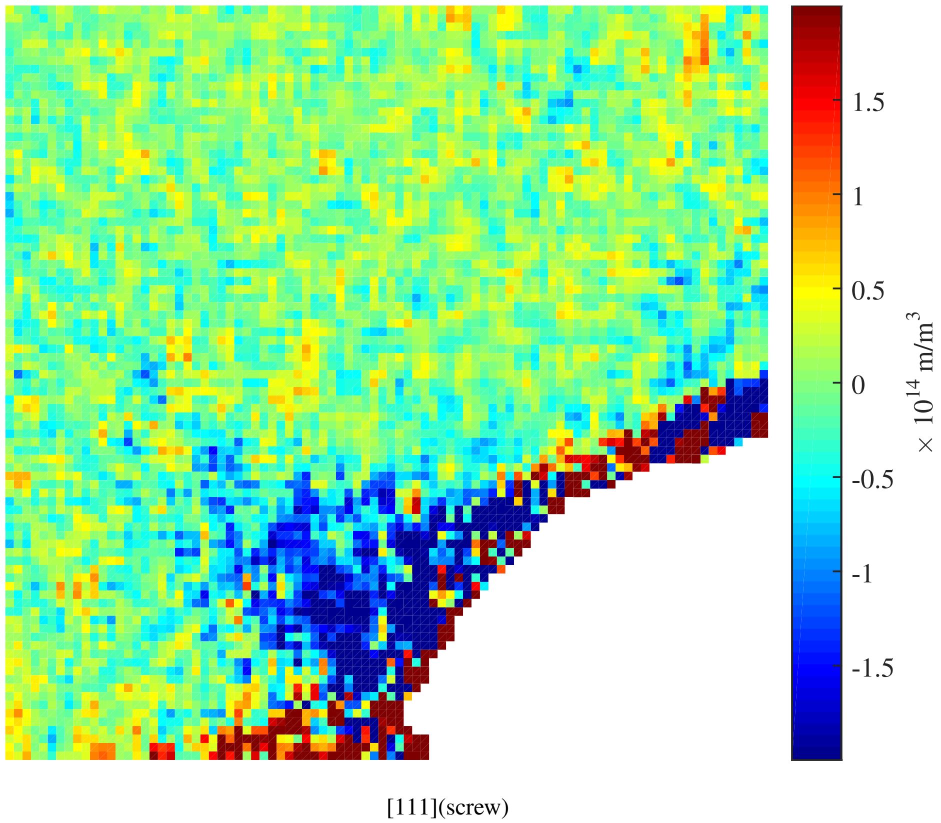

Figure 7: Dislocation density of the screw dislocations with a Burgers vector of [111] determined by CC-EBSD.

A few caveats apply when employing the Nye-Kröner method at the limits of its spatial and dislocation density resolution (i.e. when there are countably few dislocations per area resolution). First, all dislocation content is assumed to be a linear superposition of pure edge or pure screw dislocations. This means that dislocations of mixed character will be represented by superimposed fields. Additionally, at these low step sizes, noise effects are more dominant [22]. One caveat often mentioned when interpreting dislocation density fields measured via CC-EBSD is not particularly cogent at the extremes of its resolution: the Nye-Kröner method only detects geometrically necessary dislocations. Because the length scale of the scan approaches that of dislocation dipole spacing, virtually all of the dislocations in the scan area may be thought of as geometrically necessary. Despite the challenges of employing CC-EBSD dislocation characterization at a resolution suitable for comparison at the same length scale, the level of agreement with ECCI is striking.

4. Discussion

Qualitatively, there is good agreement between hotspots of the CC-EBSD GND results and the locations of individual dislocations measured from ECCI. ECCI, however, has superior spatial resolution, which allows for individual dislocations to be detected within a single grid square while data from CC-EBSD is more diffuse and noisy. The diffusivity and noise from CC-EBSD is due to the fact that a dislocation is treated as a continuum based on the strain field in the lattice, causing the limited resolution of CC-EBSD to be controlled by the original step size at which the EBSD data was acquired and the effective step size at which the GND map was calculated. While ECCI has advantages for identifying individual dislocations at low densities, CC-EBSD is advantageous because it is able to detect large lattice rotations and observe dislocations in high deformation regions that are too densely packed for ECCI, i.e. around the rim of the indent.

To obtain a more robust quantitative comparison of the measurements presented in Fig. 3, dislocation densities measured via ECCI and CC-EBSD were averaged for five separate regions. In regions 1, 2, and 3, ECCI and CC-EBSD both detected dislocations, in region 4 only ECCI observed distinct dislocations, and in region 5 no dislocations were observed using ECCI. For each of these five regions, an average GND density from CC-EBSD was determined by averaging the GND density associated with each pixel in the region, and presented in Table 1. Dislocation densities from ECCI were determined by counting the number of dislocation intersections with the surface. Dislocations were initially assumed to have line directions perpendicular to the surface, but if dislocations are not normal to the counting area, dislocation densities are underestimated [26]. To obtain corrected densities, the dislocation density should be multiplied by $\frac{1}{\cos(\theta)}$, where θ is the angle between the line direction and the beam axis. Most of the dislocations in regions 1 and 4 were identified as [1 1 1] screw dislocations with a line direction 40° to the beam axis when the sample was in the channeling condition for the ECC image in Fig. 3a. The dislocations for regions 2 and 3 were not identified and are not all the same dislocation type but many of these dislocations are likewise inclined. Since all line directions are possible, averaging the angles of the 22 possible line directions (12 for {1 1 0} slip plane systems, 6 for {1 1 2} slip plane systems, and 4 for screw dislocations) make with the beam axis, an average angle of 58° has been used for calculating the dislocation density. For all five regions, Table 1 presents both the initial and line direction corrected dislocation densities.

Due to the spatial resolution limitations of CC-EBSD as compared to ECCI, it is possible

Table 1: Comparison of CC-EBSD GND densities and ECCI dislocation densities for the 5 regions in Fig. 3.

Region #	CC-EBSD GND Density	ECCI Density	ECCI (Line Direction Correction)	ECCI (Dipole Correction)
1	$2.6 \cdot 10^{14}\,m^{-2}$	$1.6 \cdot 10^{14}\,m^{-2}$	$2.1 \cdot 10^{14}\,m^{-2}$	$1.9 \cdot 10^{14}\,m^{-2}$
2	$2.1 \cdot 10^{14}\,m^{-2}$	$8.6 \cdot 10^{13}\,m^{-2}$	$1.6 \cdot 10^{14}\,m^{-2}$	No Dipoles
3	$1.7 \cdot 10^{14}\,m^{-2}$	$1.1 \cdot 10^{14}\,m^{-2}$	$2.2 \cdot 10^{14}\,m^{-2}$	No Dipoles
4	$6.4 \cdot 10^{13}\,m^{-2}$	$6.1 \cdot 10^{13}\,m^{-2}$	$8.0 \cdot 10^{13}\,m^{-2}$	No Dipoles
5	$5.2 \cdot 10^{13}\,m^{-2}$	$0\,m^{-2}$	$0\,m^{-2}$	No Dipoles

that dipole dislocation pairs will fall within a given CC-EBSD step, canceling the contribution to the dislocation density, i.e. on the local scale ECCI may resolve dipoles while CC-EBSD may not. Significant dipole pairs are observed in the ECC images, for example in the small oval in Fig. 3a. ECCI shows 22 dislocations in region 1 with one dislocation displaying reversed contrast (i.e. opposite Burgers vectors). From the CC-EBSD perspective this dislocation will cancel out with another closely spaced dislocation and neither will be accounted for, leaving a net 20 dislocations in the CC-EBSD determined dislocation density. This effect is accounted for in the Dipole Correction Column in Table 1. Dipoles were observed in region 1, but not observed in regions 2 through 5.

The total dislocation density is made up of both GNDs and SSDs. Thus, as ECCI images reveal both the GNDs and SSDs, one would expect that the ECCI measured density would be greater than or equal to that determined by CC-EBSD. However, the results presented here do not reflect this for regions 1 and 2. This may indicate that the comparison here is being carried out in regions where the CC-EBSD GND density measurements are close to their noise floor. Indeed, region 5 is an area where no dislocations were observed using ECCI, but the CC-EBSD indicated a GND density average of $5.2 \cdot 10^{13}\,m^{-2}$. This noise floor is near the CC-EBSD GND density noise range suggested by the work of Jiang et al. [27] in which they measured the GND density noise on single crystal Si. This noise is likely due to binning/resolution of the EBSD camera [27], pattern quality due to EBSD scan rate [28], and the EBSD step size/effective step size [22, 29]. Errors may also be associated with increased diffusiveness of the EBSD patterns taken from areas with a higher density of dislocations, but it would be expected that this error would be averaged out over a number of EBSD steps. Nevertheless, if the noise level indicated by region 5 outlines an uncertainty level that is then applied to the measurements in the other regions, the CC-EBSD and ECCI measurements appear quite close.

ECCI could also result in lower measured dislocation densities simply because some dislocations may be in a zero contrast condition for the particular 2-beam channeling condition used, i.e. $\mathbf{g} \cdot \mathbf{b} = 0$ and/or $\mathbf{g} \cdot \mathbf{b} \times \mathbf{u} = 0$. In this work, however, this was not the case as this effect was accounted for by taking images at multiple channeling conditions and other dislocations do not appear. CC-EBSD will never have dislocations that are "missed" due to this effect and will be able to identify all of the dislocations that contribute to the GNDs.

Another potential limitation of ECCI is that at higher dislocation densities it becomes impossible to resolve the individual dislocations. This appears to be the case for the regions close to the indent that appear very bright. CC-EBSD does in fact identify higher dislocation density pixels in this near-indent region that appear only bright in ECCI. Overall, both CC-EBSD and ECCI have some inherent limitations to determining dislocation densities, and users should be aware of these restrictions when using these techniques.

5. Conclusions

In summary, ECCI and CC-EBSD reveal very similar dislocation distributions associated with nanoindentation deformation. While there is not a one-to-one correlation between maps from these two techniques, the dislocation densities measured by ECCI are generally similar to those determined by CC-EBSD. The discrepancies between the two techniques may be in part due to inferior spatial resolution of CC-EBSD, allowing for CC-EBSD to miss dipole arrangements, and the potential for ECCI to miss dislocations that are either under invisibility conditions or are in areas that have too many dislocations to image. Despite these minor discrepancies, the strong correlation in distributions, densities, and characterization of dislocations determined by the two techniques suggest that CC-EBSD can be used with confidence for characterizing GND structures with higher dislocation densities than those that can be imaged using ECCI. At the other extreme, this work suggests that CC-EBSD has the potential to resolve individual dislocations but cannot do so at this time with high confidence in deformed metallic materials.

The research was supported by the US Department of Energy through grant numbers DE-FG02-09ER46637 and DE-SC0012587, as well as support from Sandia National Lab.

References

[1] E. Ruedl, P. Delavignette, S. Amelinckx, Electron microscopic study of dislocations and fission damage in platinum foils, Journal of Nuclear Materials 6 (1) (1962) 46–68. doi:10.1016/0022-3115(62)90215-5.

[2] W. J. Tunstall, P. B. Hirsch, J. Steeds, Effects of surface stress relaxation on the electron microscope images of dislocations normal to thin metal foils, Philosophical Magazine 9 (97) (1964) 99–119. doi:10.1080/14786436408217476.

[3] P. Morin, M. Pitaval, D. Besnard, G. Fontaine, Electron–channelling imaging in scanning electron microscopy, Philosophical Magazine A 40 (4) (1979) 511–524. doi:10.1080/01418617908234856.

[4] D. C. Joy, D. E. Newbury, D. L. Davidson, Electron channeling patterns in the scanning electron microscope, Journal of Applied Physics 53 (8) (1982) R81–R122. doi:10.1063/1.331668.

[5] B. A. Simkin, M. A. Crimp, An experimentally convenient configuration for electron channeling contrast imaging, Ultramicroscopy 77 (1-2) (1999) 65–75. doi:10.1016/S0304-3991(99)00009-1.

[6] M. A. Crimp, Scanning electron microscopy imaging of dislocations in bulk materials, using electron channeling contrast, Microscopy Research and Technique 69 (2006) 374–381. doi:10.1002/jemt.20293.

[7] H. Mansour, J. Guyon, M. A. Crimp, N. Gey, B. Beausir, N. Maloufi, Accurate electron channeling contrast analysis of dislocations in fine grained bulk materials, Scripta Materialia 84-85 (2014) 11–14. doi:10.1016/j.scriptamat.2014.03.001.

[8] S. Zaefferer, N.-N. Elhami, Theory and application of electron channelling contrast imaging under controlled diffraction conditions, Acta Materialia 75 (2014) 20–50. doi:10.1016/j.actamat.2014.04.018.

[9] T. J. Ruggles, D. T. Fullwood, Estimations of bulk geometrically necessary dislocation density using high resolution EBSD, Ultramicroscopy 133 (2013) 8–15. doi:10.1016/j.ultramic.2013.04.011.

[10] A. J. Wilkinson, G. Meaden, D. J. Dingley, High-resolution elastic strain measurement from electron backscatter diffraction patterns: New levels of sensitivity, Ultramicroscopy 106 (4-5) (2006) 307–313. doi:10.1016/j.ultramic.2005.10.001.

[11] A. J. Wilkinson, E. E. Clarke, T. B. Britton, P. Littlewood, P. S. Karamched, High-resolution electron backscatter diffraction: an emerging tool for studying local deformation, Journal of Strain Analysis for Engineering Design 45 (5) (2010) 365–376. doi:10.1243/03093247JSA587.

[12] J. R. Seal, T. R. Bieler, M. A. Crimp, T. B. Britton, A. J. Wilkinson, Characterizing Slip Transfer In Commercially Pure Titanium Using High Resolution Electron Backscatter Diffraction (HR-EBSD) and Electron Channeling Contrast Imaging (ECCI), Microscopy and Microanalysis 18 (S2) (2012) 702–703. doi:10.1017/S1431927612005363.

[13] J. Guyon, H. Mansour, N. Gey, M. A. Crimp, S. Chalal, N. Maloufi, Sub-micron resolution selected area electron channeling patterns, Ultramicroscopy 149 (2015) 34–44. doi:10.1016/j.ultramic.2014.11.004.

[14] V. I. Nikolaichick, I. I. Khodos, A review of the determination of dislocation parameters using strong- and weak-beam electron microscopy, Journal of Microscopy 155 (2) (1989) 123–167. doi:10.1111/j.1365-2818.1989.

tb02879.x.
URL http://doi.wiley.com/10.1111/j.1365-2818.1989.tb02879.x

[15] J. Ahmed, A. J. Wilkinson, S. G. Roberts, Study of dislocation structures near fatigue cracks using electron channelling contrast imaging technique (ECCI), Journal of Microscopy 195 (3) (1999) 197–203. doi:10.1046/j.1365-2818.1999.00574.x.

[16] D. Hull, D. J. Bacon, Introduction to Dislocations, Butterworth-Heinemann, 2001.

[17] J. F. Nye, Some geometrical relations in dislocated crystals, Acta Metallurgica 1 (2) (1953) 153–162. doi:10.1016/0001-6160(53)90054-6.

[18] F. Ram, Z. Li, S. Zaefferer, S. M. Hafez Haghighat, Z. Zhu, D. Raabe, R. C. Reed, On the origin of creep dislocations in a Ni-base, single-crystal superalloy: an ECCI, EBSD, and dislocation dynamics-based study, Acta Materialia 109 (2016) 151–161. doi:10.1016/j.actamat.2016.02.038.

[19] A. Vilalta-Clemente, G. Naresh-Kumar, M. Nouf-Allehiani, P. Gamarra, M. A. Di Forte-Poisson, C. Trager-Cowan, A. J. Wilkinson, Cross-correlation based high resolution electron backscatter diffraction and electron channelling contrast imaging for strain mapping and dislocation distributions in InAlN thin films, Acta Materialia 125 (2017) 125–135. doi:10.1016/j.actamat.2016.11.039.

[20] S. Zaefferer, New developments of computer-aided crystallographic analysis in transmission electron microscopy, Journal of Applied Crystallography 33 (2000) 10–25.

[21] Brigham Young University, OpenXY (2016).
URL https://github.com/BYU-MicrostructureOfMaterials/OpenXY

[22] T. J. Ruggles, T. M. Rampton, A. Khosravani, D. T. Fullwood, The effect of length scale on the determination of geometrically necessary dislocations via EBSD continuum dislocation microscopy, Ultramicroscopy 164 (2016) 1–10. doi:10.1016/j.ultramic.2016.03.003.

[23] Y. N. Picard, M. E. Twigg, J. D. Caldwell, C. R. Eddy Jr., M. A. Mastro, R. T. Holm, Resolving the Burgers vector for individual GaN dislocations by electron channeling contrast imaging, Scripta Materialia 61 (8) (2009) 773–776. doi:10.1016/j.scriptamat.2009.06.021.

[24] G. Naresh-Kumar, B. Hourahine, P. R. Edwards, A. P. Day, A. Winkelmann, A. J. Wilkinson, P. J. Parbrook, G. England, C. Trager-Cowan, Rapid Nondestructive Analysis of Threading Dislocations in Wurtzite Materials Using the Scanning Electron Microscope, Physical Review Letters 108 (13). doi:10.1103/PhysRevLett.108.135503.

[25] T. J. Ruggles, D. T. Fullwood, J. W. Kysar, Resolving geometrically necessary dislocation density onto individual dislocation types using EBSD-based continuum dislocation microscopy, International Journal of Plasticity 76 (2016) 231–243. doi:10.1016/j.ijplas.2015.08.005.

[26] M. Crimp, J. Hile, T. Bieler, M. Glavicic, Dislocation density measurements in commercially pure titanium using electron channeling contrast imaging, TMS Letters 1 (2004) 15–16.

[27] J. Jiang, T. B. Britton, A. J. Wilkinson, Measurement of geometrically necessary dislocation density with high resolution electron backscatter diffraction: Effects of detector binning and step size, Ultramicroscopy 125 (2013) 1–9. doi:10.1016/j.ultramic.2012.11.003.

[28] T. B. Britton, J. Jiang, R. Clough, E. Tarleton, A. I. Kirkland, A. J. Wilkinson, Assessing the precision of strain measurements using electron backscatter diffraction – part 1: Detector assessment, Ultramicroscopy 135 (2013)

126–135. doi:10.1016/j.ultramic.2013.08.005.

[29] B. Adams, J. Kacher, EBSD-Based Microscopy: Resolution of Dislocation Density 14 (3) (2009) 185–196.